

## Body-force model comparison of plasma flows induced by DBD plasma actuator in quiescent air

oChen Di, Tokyo University of Science, 6-3-1 Nijuku, Katsushika, Tokyo 125-8585, chendi@rs.tus.ac.jp

Asada Kengo, (as above), asada@rs.tus.ac.jp

Sekimoto Satoshi, (as above), a28032@rs.tus.ac.jp

Hiroyuki Nishida, Tokyo University of Agriculture and Technology, Koganei, Tokyo 184-8588, hnishida@cc.tuat.ac.jp

Fujii Kozo, Tokyo University of Science, 6-3-1 Nijuku, Katsushika, Tokyo 125-8585, fujii@rs.tus.ac.jp

Numerical simulations of two-dimensional plasma flows induced by dielectric barrier discharge plasma actuators in quiescent air are conducted with two different body force models: Suzen-Huang (S-H) model and drift-diffusion (D-D) model. At the low peak-to-peak voltage of 7kV, the D-D model shows high maximum induced velocity, however, more compact body force distribution and less driven flow than that of the S-H model with  $D_c = 0.0117$ , which was experimentally validated. Through the horizontal velocity fields and the momentum increment, the results show that the D-D model at 10kV generates the most similar flow field to the S-H model only in the downstream region of the covered electrode, where the induced flow structure is not fully developed because of the insufficient computational time.

### 1. Introduction

Active flow control utilizing plasma generators has raised much interest for its high availability and feasibility, dielectric barrier discharge plasma actuator (DBD-PA) is such a typical device for flow control, which only consists of two electrode and a dielectric layer between them, see Fig. 1(a). Due to the thin and light structure, DBD-PA can be attached on any flat or curved surfaces, corner or edge, where flow separation control is considered,<sup>1,4</sup> more importantly, without changing the original shape of an object. In recent 20 years, an increasing number of studies are conducted not only on separation control in Fig. 1(b,c), but also on noise reduction,<sup>5</sup> drag reduction<sup>6</sup> and flow transition delay.<sup>7</sup>

DBD-PA, in this paper a single asymmetric DBD-PA as we concerned, typically can generate a wall jet with the maximum velocity up to around 10m/s when the voltage and the base frequency of operating alternating current (AC) is 5-20kV (peak to peak) and 1-10kHz respectively. The ionization effect is largely determined by the applied voltage as well as the electric permittivity of dielectric layer. The mechanism of plasma-assisting flow control is believed as follows, the interaction of the ionized gas and neutral air result in an electrohydrodynamic body-force vector field coupling with the momentum transfer in the external flow at the downstream of the exposed electrode.<sup>8-11</sup>

To understand the flow phenomena with the plasma-induced body force, many research have made a great effort on the body-force modelling,<sup>4,12-14</sup> specifically, the spatio-temporal distribution of the body force, which can be incorporated into high-fidelity flow simulation.<sup>27,15,16</sup> The early models for body force field generated by a single DBD-PA, proposed by Massines et al.<sup>12</sup> and Roth et al.,<sup>13</sup> are one-dimensional (1-D) based on static formulation and does not account for the presence of the charged particles, therefore it barely fit to 2-D or 3-D applications. Furthermore, several semiempirical models of 2-D plasma flow modelling, using linear,<sup>14</sup> exponential functions,<sup>10,11</sup> and Gaussian distribution<sup>4</sup> of the spatial decay for the 2D body force component are reviewed by Corke et al.<sup>17</sup>

Experimental methods to investigate the body force production are largely employed with the flow measurement technics, the body force vector can be determined in Navier-Stokes momentum equation with the measured velocity,<sup>18,19</sup> using particle image velocimetry (PIV) and laser

doppler velocity (LDV).

Simulation-assisted studies including simple analytical models are mainly discussed in current paper. Suzen and his colleagues<sup>4</sup> proposed the electrostatic model as the following equation derived from Enloe et al.'s,<sup>10</sup>

$$\mathbf{f}_i = Q_c \mathbf{E}_i = Q_c (-\nabla \phi), \quad (1)$$

where  $\mathbf{f}_i$  and  $\mathbf{E}_i$  denotes body force vector and electric field vector, respectively. The force is contributed by two different parts: the external electric potential  $\phi$  and the electric field created by the net charged density  $Q_c$ . The net body-force obtained by the analytical solution of Suzen-Huang (S-H) model is well validated by the experimental results,<sup>20</sup> however, the model ignored the complex plasma chemistry which leads to the highly unsteady forcing on the plasma flow.

In contrast, the charged-particle models associated with the first-principles fully-coupled approaches, considered the ordinary force diffusion, drift motion and Coulomb acceleration of electrons, and positive and negative ions, respectively. The so-called drift-diffusion (D-D) model was first developed for the physical modelling,<sup>21-23</sup> which focused on the electric-field effects on the charged particles. More recently, in spite of the time-consuming computing, D-D model was widely applied in the simulation of DBD-PA induced body-force field,<sup>9,24</sup> however, few researches have input the D-D body force into flow simulation. Gaitonde et al.<sup>25</sup> conducted plasma-based stall control simulations with coupled first-principles approaches that largely reduced the complexity of the broad-spectrum problem. Nonetheless, the induced flow field of high temporal resolution during a single discharge cycle still remains unclear.

On the other hand, the analytical S-H models<sup>4</sup> and Shyy models<sup>14</sup> of low temporal resolution are well incorporated into the numerical flow simulations of Asada et al.<sup>15,16,20</sup> and Visbal et al.<sup>27</sup> for their simplicity. The extra body force term in the Navier-Stokes equations include the parameter  $D_c$  representing the scaling of the electrical to inertial forces.  $D_c$  from another perspective describes the strength of body force, however, it is given empirically for each case considered. As to the transient accuracy of DBD-PA-induced flow, the S-H model utilizes the smooth and symmetrical sinusoidal function, while the D-D model shows the totally different discharge density in positive-going and negative-going phase of the applied AC power,<sup>24</sup> which is more reliable as it matches better with the

experimental observation.<sup>26</sup>

To investigate the effect of the sophisticated D-D model on the high-resolution flow simulations, this research carries out a comparison between the D-D model and the S-H model in quiescent air, of which the latter one has been largely employed in our previous research.<sup>15,16,20</sup>

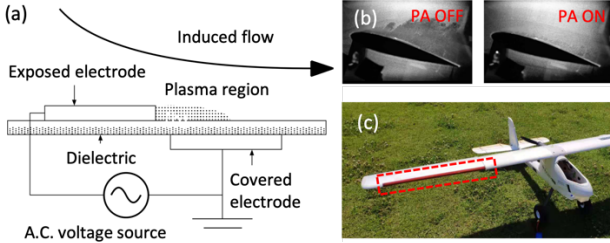


Fig. 1. (a) Sketch of DBD-PA, (b) wind tunnel test on airfoil, figures adapted with permission from Fujii (2018).<sup>27</sup> (c) DBD-PA attached on the leading edge of a small model plane, figures shot in a flight test.

## 2. Methodology

### 2.1. Governing equations of fluid dynamics

The near-wall flow field driven by the plasma flow of DBD-PA in the quiescent air is described by the two-dimensional (2D) compressible Navier-Stokes equations, augmented by the terms representing the local forcing on the ionized region above a flat plate. The non-dimensional forms of the continuity, momentum, and energy equations, as well as the ideal gas equation are written as

$$\frac{\partial \rho}{\partial t} + \frac{\partial \rho u_k}{\partial x_k} = 0, \quad (2)$$

$$\frac{\partial \rho u_i}{\partial t} + \frac{\partial (\rho u_i u_k + p \delta_{ik})}{\partial x_k} = \frac{1}{\text{Re}} \frac{\partial \tau_{ik}}{\partial x_k} + D_c S_i, \quad (3)$$

$$\frac{\partial e}{\partial t} + \frac{\partial ((e+p)u_k)}{\partial x_k} = \frac{1}{\text{Re}} \left( \frac{\partial u_l \tau_{kl}}{\partial x_k} - \frac{1}{(\gamma-1)\text{Pr}M_\infty^2} \frac{\partial q_k}{\partial x_k} \right) + D_c S_k u_k \quad (4)$$

$$p = (\gamma - 1)(e - 0.5 \rho u_k u_k) \quad (5)$$

where  $\mathbf{x}_i$  represents the position vector,  $\mathbf{u}_i$  the velocity vector,  $\mathbf{q}_k$  the heat flux vector,  $\rho$  the density,  $p$  the static pressure,  $e$  the total energy per unit volume,  $\tau_{ik}$  the stress tensor,  $\delta_{ij}$  the Kronecker delta,  $\mathbf{S}_i$  the body force vector,  $\gamma$  the ratio of specific heats,  $t$  the time. In 2-D Cartesian system, the subscript  $i, k, l$  denotes the wall-parallel and wall-normal direction. The above terms are all non-dimensional, the body force term  $\mathbf{S}_i$  is normalized by

$$\mathbf{S}_i = \frac{1}{\rho_{\text{ref}} U_{\text{ref}}^2} \mathbf{f}_i, \quad (6)$$

where the net force  $\mathbf{f}_i$  is computed in Eqn. (1).

$D_c$  is the non-dimensional parameter, representing the ratio of the electrical force of the fluid to its inertial force, see details in the next section. In addition, the Reynolds number (Re), the Prandtl number (Pr), and the Mach number ( $M_\infty$ ), are defined as follows,

$$\text{Re} = \frac{\rho_{\text{inf}} U_{\text{inf}} L_{\text{inf}}}{\mu_{\text{inf}}}, \text{Pr} = \frac{\mu_{\text{inf}} C_p}{\kappa_{\text{inf}}}, M_\infty = \frac{U_{\text{inf}}}{a_{\text{inf}}} \quad (7)$$

where  $\mu$  is the viscosity,  $L$  is the length,  $U$  is the velocity,  $a_{\text{ref}}$  is the speed of sound,  $C_p$  is the specific heat at constant pressure, and  $\kappa_{\text{inf}}$  is the thermal conductivity; the subscript inf indicates the reference values.

### 2.2. Suzen-Huang body force model

In this section, the spatial distribution of body force  $\mathbf{S}_i$  in Eqn. (3) and (4) is presented by S-H model.<sup>4</sup> As we introduced from Eqn. (1), the

body force vector is computed by multiplying the charge density  $Q_c$  and electric field vector  $\mathbf{E}_i$ , which are solved in the Maxwell's equations of the external electric potential  $\phi$  and the charged particle potential, respectively, as follows:

$$\nabla \cdot (\epsilon_r \nabla \phi) = 0, \quad (8)$$

$$\nabla \cdot (\epsilon_r \nabla Q_c) = \frac{Q_c}{\lambda_d^2}, \quad (9)$$

where  $\epsilon_r$  denotes the relative permittivity of the dielectric layer, and  $\lambda_d$  denotes the Debye length. The boundary conditions of Eqn. (8) at the exposed electrode and Eqn. (9) on the wall above the covered electrode are shown in Fig. 2(b), can be written as

$$\phi(t) = \phi^{\text{max}} f(t), \quad (10)$$

$$Q_{c,w}(x, t) = Q_c^{\text{max}} G(x) f(t), \quad (11)$$

respectively, where  $\phi^{\text{max}}$  and  $Q_c^{\text{max}}$  are the maximum values of the external electric potential and the charge density, respectively. These two parameters controlling the strength of the plasma actuator's effects can be calibrated using available experimental data.<sup>10</sup>

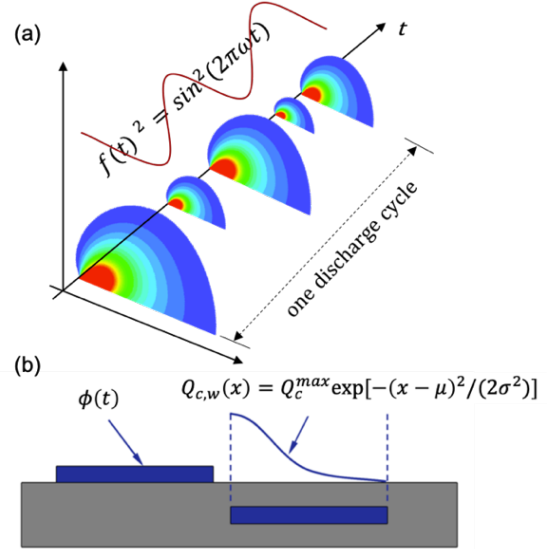


Fig. 2. (a) Spatial and temporal distribution of body force in S-H model. (b) Boundary condition of charged particle in S-H model, following a half Gaussian distribution.<sup>4</sup>

The spatial distribution of the charged particles is given by a half Gaussian function  $G(x)$  and the temporal variation of both Eqn. (10) and (11) can be a sine wave form  $f(t) = \sin^2(2\pi\omega t)$ , here  $\omega$  is the base frequency of AC power, therefore  $|\mathbf{f}_i| \propto \sin^2(2\pi\omega t)$ , as it is described in Fig. 2(a).

After substituting the solution of Eqn. (8) and (9) into Eqn. (1) and (6), we obtain the non-dimensional body force  $\mathbf{S}_i$ , of which the magnitude is represented by multiplying the non-dimensional parameter  $D_c$ , here it is defined as

$$D_c = \frac{Q_c^{\text{max}} E^{\text{max}} L_{\text{ref}}}{\rho_{\text{ref}} U_{\text{ref}}^2}, \quad (12)$$

$E^{\text{max}} = (-\nabla \phi^{\text{max}})$  and  $Q_c^{\text{max}}$  are the maximum magnitude of the electric field vector and the particle charge, respectively. To choose the appropriate  $D_c$  value, Aono et al.<sup>20</sup> conducted many comparison cases between the experiments and the pre-computation of the S-H model.

### 2.3. Two-dimensional drift-diffusion model

Notwithstanding the capability of the D-D model in 3D body force

simulation by Nishida et al.,<sup>24</sup> in this study we conduct the model comparison in 2D simulation for convenience and simplicity. We consider the electron, the positive ion, and the negative ion with a basic plasma chemistry including electron impact ionization, attachment, and recombination. The time-dependent continuity equations for electron and ions with a D-D flux are coupled with Poisson equation. The governing equations are written as,

$$\frac{\partial n_e}{\partial t} + \nabla \cdot (-n_e \mu_e \mathbf{E} - D_e \nabla n_e) = (\alpha - \eta) n_e |v_e| - r_{ep} n_e n_p, \quad (13)$$

$$\frac{\partial n_p}{\partial t} + \nabla \cdot (n_p \mu_p \mathbf{E} - D_p \nabla n_p) = \alpha n_e |v_e| - r_{ep} n_e n_p - r_{pn} n_p n_n, \quad (14)$$

$$\frac{\partial n_n}{\partial t} + \nabla \cdot (-n_n \mu_n \mathbf{E} - D_n \nabla n_n) = \eta n_e |v_e| - r_{pn} n_p n_n, \quad (15)$$

$$\nabla \cdot (\epsilon_r \mathbf{E}) = \frac{e}{\epsilon_0} (n_p - n_e - n_n) + \frac{e}{\epsilon_0} \sigma \delta_s, \quad (16)$$

where  $n$  is the plasma density,  $\mu$  is the charged particle mobility, and their subscript  $e, p, n$  denote the electron, the positive ion, and the negative ion,  $D, \alpha$  and  $\eta$  are the coefficients of diffusion, ionization and attachment,  $r_{ep}$  and  $r_{pn}$  are the recombination coefficients of electron-positive-ion and positive-negative-ion, respectively. In Eqn. (15),  $e$  is the elementary charge,  $\sigma$  is the surface charge density similar to the boundary condition of  $Q_{c,w}$  in Eqn. (10), here it is expressed by the Dirac function  $\delta_s$ .  $\epsilon_0$  and  $\epsilon_r$  are the vacuum and relative permittivity of the dielectric layer, respectively. The ionization and attachment coefficients and electron mobility are calculated by the BOLSIG<sup>28</sup> simulation software assuming the ambient gas is air ( $N_2:O_2 = 0.8:0.2$ ). Other coefficients and parameters, partly shown in Fig. 3(b) keep the same with the work of Nishida et al.<sup>24</sup>

In the computation of electrohydrodynamic (EHD) force, as we call the body force, can be obtained by solving Eqn. (12-15), see details in the previous work of Nishida et al..<sup>9,24,29</sup> With the assumption in the previous studies, the body force is equal to the rate of momentum transfer per unit volume due to collisions,<sup>22,23,29</sup>

$$\mathbf{f} = e(n_p - n_e - n_n) \mathbf{E} - \left[ \frac{D_p}{\mu_p} \nabla n_p + \frac{D_e}{\mu_e} \nabla n_e + \frac{D_n}{\mu_n} \nabla n_n \right], \quad (17)$$

on the right side, the first term of which is dominant in current condition, also correspond to that in Eqn. (1). Therefore, the unipolar region of the discharge plasma is the main region which contributes to the EHD force.

#### 2.4 Numerical approaches

To solve the 2D Navier-Stokes equations in Eqn. (2)-(5), we employ a compressible fluid analysis solver, LANS3D.<sup>30,31</sup> In the present research, all the spatial derivatives are obtained with a sixth-order compact difference scheme,<sup>32</sup> and lower-upper symmetric alternating direction implicit and symmetric Gauss-Seidel (ADI-SGS)<sup>33</sup> method is utilized for time integration. Near the boundary, second-order explicit difference schemes are used because of the unavailability of high-order compact difference scheme. Tenth-order filtering<sup>32</sup> is applied with a filtering coefficient of 0.42. The non-dimensional time increment, which is normalized by the reference velocity and chord length, is set to  $1 \times 10^{-5}$  in order to match the input frequency of the transient body force of the D-D model. Correspondingly, the Courant-Friedrichs-Lewy (CFL) number is less than approximately 2.0. On the surface of the flat plate, no-slip and adiabatic conditions are imposed. At the inlet, zero velocities are assigned.

As to the body force computing in the D-D model, our current work largely follows the work of Nishida et al..<sup>9,24,29</sup> The drift terms in Eqn. (13)–(15) are evaluated by the upwind scheme using the MUSCL interpolation, and the diffusion terms are evaluated by the central difference scheme. The Poisson equation (16) is solved by the successive over-relaxation (SOR) method with the semi-implicit technique. The time integration is conducted by the implicit scheme, with the constant time increment of  $2 \times 10^{-10}$  [s], which is less than the adaptive value using CFL condition in<sup>24,29</sup>. Due to the complexity of the charged-particle simulation, the timestep of D-D model is several orders smaller than that of computational fluid dynamics (CFD). We compute 4.5 discharge circles by D-D model, and select 3 periods ( $1.25T_{base}$  to  $4.25T_{base}$ ) for phase-averaging input, which contains 1000 transient body force fields in one discharge cycle, while the S-H model employs a sine-varying body force field for transient input, see Fig. 2(a). The timestep of the input frequency matches that in CFD simulation in real scale.

The 2D computational domains and grids are shown in Fig. 3(a), including the body-force computation and CFD, of which the grid resolutions are  $600 \times 250$  (red frame) and  $873 \times 416$  (background), respectively. The sensitivity tests of grid resolution in both cases were well implemented in the previous studies.<sup>30,24</sup> As to the boundary conditions in CFD, no-slip and adiabatic conditions were imposed On the surface of the flat plate, and zero velocities are assigned at the inlet. The detailed configuration of DBD-PA in the D-D computational domain is shown in Fig. 3(b).

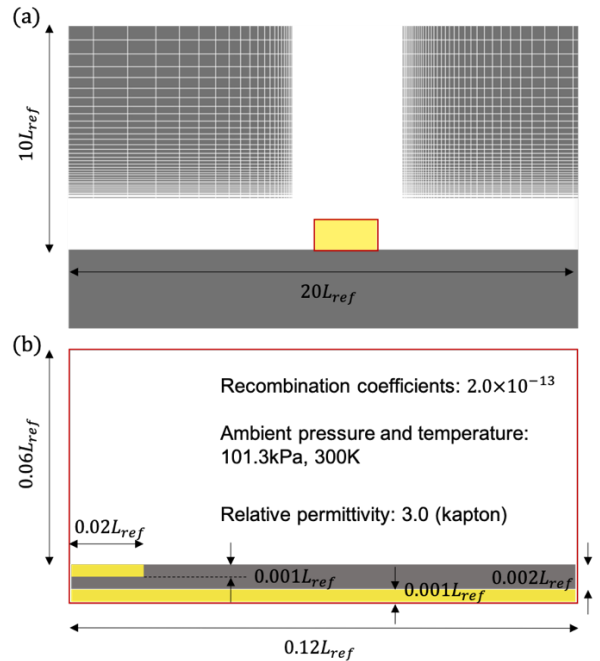


Fig. 3. (a) Domain incorporation of the body-force computation (highlighted) into CFD (background). (b) Configuration of the plasma actuator (yellow denotes the exposed and covered electrode, grey denotes the dielectric layer), and physical parameters for D-D model.

#### 2.5 Computational setup of DBD-PA

The flow field is assumed to be globally quiescent and laminar above the flat plate. The Reynolds number is 63,000, the Mach number is 0.2, the specific heat ratio ( $\gamma$ ) is 1.4, and the Prandtl number (Pr) is 0.72, assumed to be the same as those used in the previous simulation<sup>16</sup> and experiment setup.<sup>20</sup>

As it shows in Fig. 4, a sinusoidal form  $0.5V_{pp}\sin(2\pi f_{base}t)$  of AC power is applied on the electrodes, of which the peak-to-peak amplitude ( $V_{pp}$ ) is set to 7kV, 10kV, 12kV and 20kV for the D-D models, and the base frequency ( $f_{base}$ ) is 10000Hz. As to the S-H model,  $D_c$  in Eqn. (12) is set to 0.0117 in this study corresponding to  $V_{pp} = 7kV$ , of which case is experimentally validated in the previous study.<sup>20</sup>

Both continuous and burst modes are employed as the input modes of body force in D-D and S-H models. DBD-PA is permanently activated in the continuous mode, and periodically activated in the burst mode with the burst frequency  $f^+ = 500$  [Hz]. Burst ratio (BR) is 0.1, which means a single burst contains two periods of the discharge cycle. Note that  $F^+$  and  $F_{base}$  are the normalized values of burst and base frequency, respectively. All the cases simulate up to  $30T$ , it means the simulations have run 30 burst periods, 0.06s in real scale, see Fig. 4.

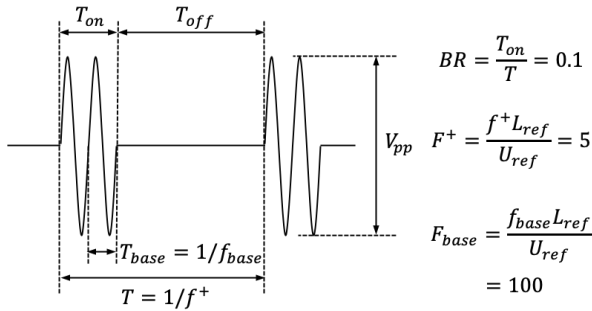


Fig. 4. Schematic diagram of a bursting wave input signal.

### 3. Results and discussions

Body force term as we show on the right side of Eqn. (3) and (4) are computed by the D-D model and the S-H model. Fig. 5 shows the first two cycles of the spatial integrated EHD force. The S-H force is proportional to the function of  $\sin(2\pi\omega t)$ , and the force peak is quite close to that of the D-D force at 10kV. The remarkable difference of the D-D forces between the positive-going and the negative-going voltage can be observed, although that of the discharge density is not shown in this study. Both positive and negative-going phases show the positive body force, which agrees with other simulation results,<sup>23,24</sup> however, in the negative-going phase it shows the much stronger instantaneous push/push forces at a few moments, the two force peaks approximately appear at both the ends of positive-going ( $2/4 T_{base}$ ) and negative-going phase ( $4/4 T_{base}$ ). Similarly, the instantaneous D-D body force fields in the right column of Fig. 6 also show that phenomenon.

Fig. 6 further compares the averaged body force distribution of the S-H model, as well as the D-D models at the varying applied voltage. The discharged area increases with the applied voltage in the D-D model, in other words, more plasma is induced with the increasing voltage. It is worthy to note that the D-D model at 7kV has a similar area of  $S_x > 0.1$  compared with that of the S-H model, however,  $S_x$  decreases faster with the distance from the end of the exposed electrode. As to the entire induced area of plasma ( $S_x > 0$ ), the area of the D-D model at 10kV is most close to that of the S-H model.

It is quite straightforward to relate the body force production with the induced flow field, especially in quiescent air. Fig. 7 shows the horizontal velocity fields in the continuous mode, computed with the pre-simulated body force of the S-H model and the D-D models. The S-H flow field experimentally corresponds to the case at 7kV, however, shows much weaker induced velocity in Fig. 7. It is probably caused by the underestimated ionization effect of D-D model at such a low applied

voltage, and also can be caused by the simplicity of the S-H model in the body force distribution. This can be remained as an open question for further optimizing the body force model. In the present study, we mainly focus on the hydrodynamic effect of the D-D model, and the D-D model at 10kV show a similar flow field as that of the S-H model better when we just look at the flow fields in Fig. 7.

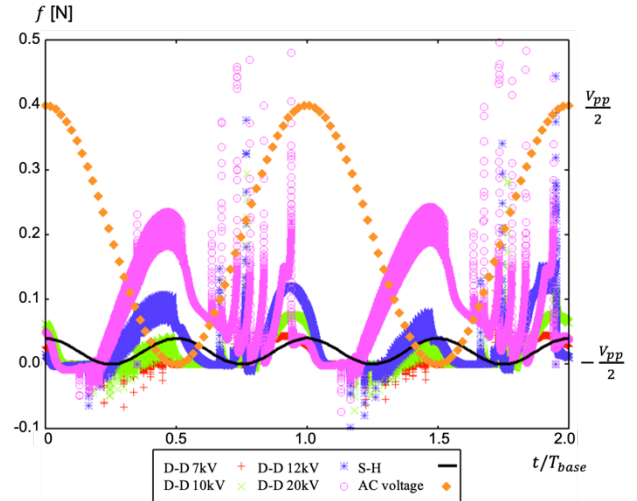


Fig. 5. Time history (two periods) of the dimensional area-integrated EHD force in the computing area, using the S-H model and the D-D model at 7kV, 10kV, 12kV and 20kV. The corresponding AC voltage is also plotted.

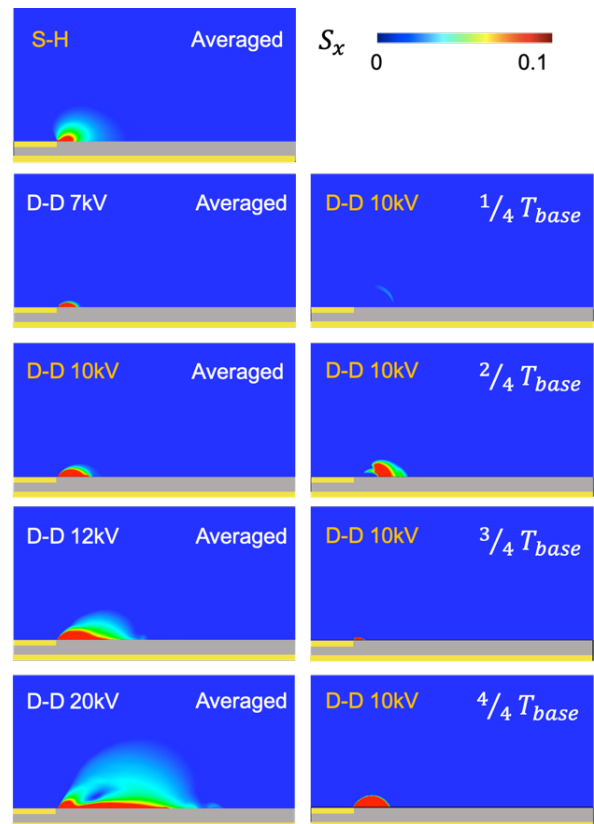


Fig. 6. Horizontal body force field in the gas layer above the entire covered electrode.  $S_x$  is the non-dimensional horizontal force. The left column is the averaged field of S-H model, and D-D model at 7kV, 10kV, 12kV, 20kV. The right column is the transient field of D-D model at 10kV.

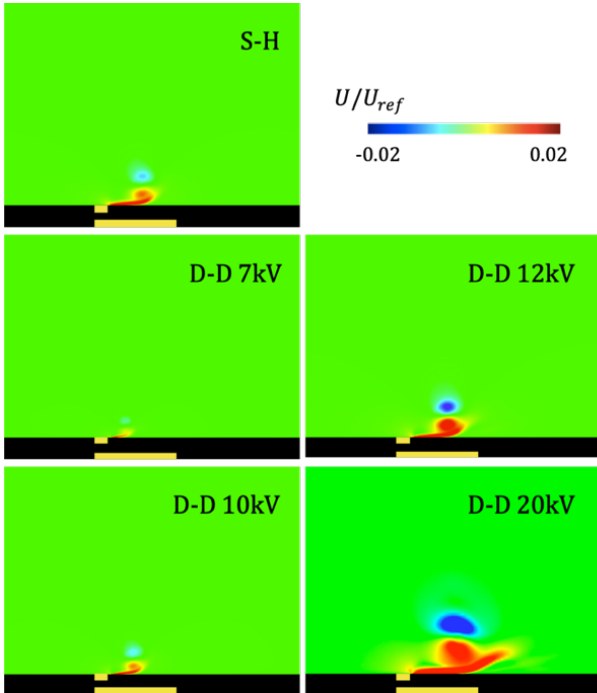


Fig. 7. Horizontal induced velocity fields obtained from CFD. Here  $U/U_{ref}$  is the non-dimensional velocity.

The flow fields in Fig. 7 seems to be quite initial states, in which the starting vortices are still in the body force domain. The vortices will keep moving to the downstream, and the flow fields achieves convergence when the induced flow becomes a steady wall jet. In this study, the time duration in current simulation is only up to 0.06s, which is far from the convergent state compared with the experiments.<sup>34</sup> The future work may spend more computational time to reach the convergent state, based on that, the comparison results may be different.

Velocity profiles in Fig. 8 show more detailed flow fields for model comparison. The results are also obtained in the continuous mode. It is obvious to see that both the S-H and the D-D models in all the cases reach the maximum velocity near  $x/L_{ref}=0.05$ , one exposed-electrode length away from the downstream edge. The velocity profiles of the D-D model at 10kV have the best agreement with those of the S-H model at most streamwise locations. At the edge of the exposed electrode  $x/L_{ref}=0$ , all the D-D cases have the local maximum velocity much closer to the wall than that of the S-H model, see the inner window. Similar to the results in Fig. 7, the velocity profile of the D-D model at 7kV still shows weak induced flow, specifically, smaller driven area compared with the S-H model with  $D_c=0.0117$ . The D-D models at 12kV and 20kV induce much stronger flow due to the larger discharge area shown in Fig. 6.

Is D-D based induced flow really weak at 7kV? As the four streamwise locations seem not to be enough for a detailed flow structure, we search the global maximum velocities in the fields, which are shown in the bottom half of Fig. 9. The global maximum velocity of the S-H case is smaller than those of all D-D cases. Moreover, in the top half of Fig. 9, the location of maximum velocity of S-H case is much further away than those of D-D cases.

In summary, we notice that the induced flow simulated by the D-D model at 7kV is not locally weak in the maximum horizontal velocity, however, due to the much smaller distribution area of body force, less flow is driven, thus the induced flow is weak in the downstream.

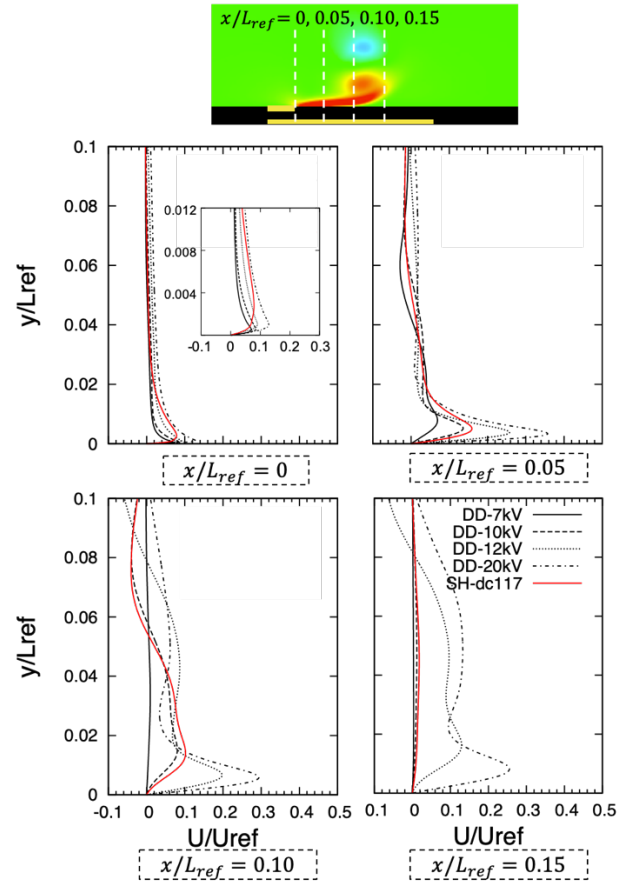


Fig. 8. Horizontal velocity profiles plotted at  $x/L_{ref}=0, 0.05, 0.10$  and  $0.15$ , these locations are showed with the white dashed lines on the top. Red line 'S-H-dc117' denotes the S-H model with  $D_c=0.0117$ , and black lines denote the D-D models at different applied voltage.

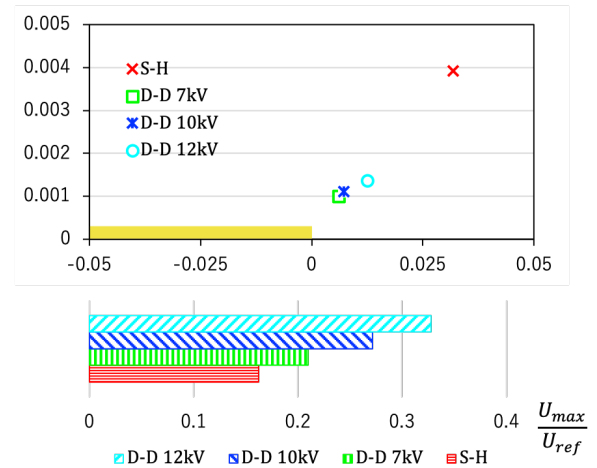


Fig. 9. Global maximum velocity (horizontal). Magnitude (lower) and location (upper) in S-H and D-D cases.

To comprehensively compare the two body force models, we consider the area integration of the induced momentum, which combines the magnitude and the distribution area of the induced flow, and is defined as follows:

$$M = \int_{x_s}^{x_e} \int_{y_s}^{y_e} \frac{1}{2} \rho \bar{U}^2(x, y) dx dy, \quad (18)$$

here  $\bar{U} = U/U_{ref}$  is the non-dimensional velocity,  $x_s, x_e, y_s, y_e$  form a

rectangular window ( $\approx 0.4L_{ref} * 0.25L_{ref}$ ) for calculating the momentum in it. The results are obtained in the simulations of burst mode, shown in Fig. 10. All the case simulates  $20T_{burst}$  from the beginning, but the D-D cases only plot the second half. Momentum increment ( $\Delta M$ ) is observed during every single burst, it can be regarded as the power input by the PA-induced body force through the computation of the D-D model and S-H model.

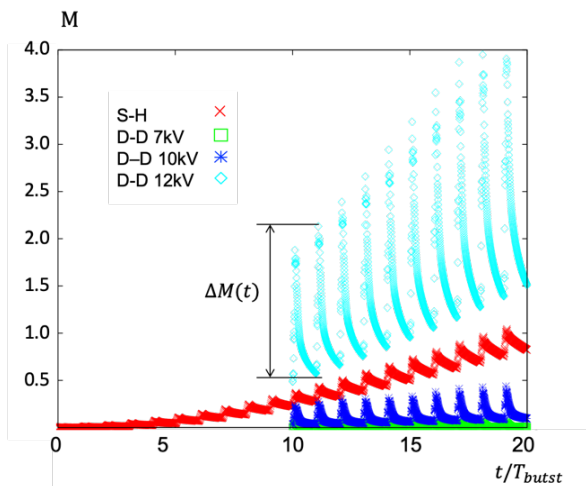


Fig. 10. Area integration of momentum ( $M$ ).

Again, as we mainly focus on the hydrodynamic effect of the two models,  $\Delta M$  is thought to be the best candidate to evaluate the body force model. Fig. 10 shows  $M$  generally increase faster in S-H case, up to  $t = 20T_{burst}$ ,  $\Delta M$  in S-H case and D-D 10kV case agrees well. The decrease of  $M$  is caused by the viscous dissipation, although D-D cases show different profiles in the decrease, this phenomenon is beyond the scope of our current study.

#### 4. Conclusion

In the present research we conduct the simulations of both the body force induced by DBD-PA and the induced flow field. As to the body force model, the Suzen-Huang model and the drift-diffusion model are compared. S-H model with  $D_c = 0.0117$  is well validated with the previous experiment,<sup>20</sup> in which the applied voltage is set to 7kV. The body force of the D-D model is more unsteady, locally stronger and the distribution is more compact than that of the S-H model. The velocity contours and the velocity profiles show that the D-D model at 10kV produces the most similar flow fields in the downstream. D-D model at 7kV generates high maximum horizontal velocity, at the location quite close to the edge of the exposed electrode, however, the driven area is much smaller than that of the S-H model. Finally, we consider the momentum increment in the burst mode of DBD-PA to evaluate the power input and the hydrodynamic effect of the two body force models. The D-D model at 10kV has the best agreement with the S-H model, while at 7kV the D-D model may underestimate the ionization effect or the three-dimensional effect,<sup>24</sup> which needs further investigation by experiments. Additionally, in order to obtain a fully developed flow field, the computational time of the present research need to be extended in the future work.

#### Acknowledgement

The present study was supported in part by the Japan Society for the Promotion of Science (JSPS) through Grants-in-Aid for Scientific Research (No. 18H03816). The computation was partly supported by the

supercomputer SX-ACE in Tohoku University. The authors also appreciated the valuable discussion with Prof. Marios Kotsonis from TU Delft.

#### Bibliography

- Post, M. L., & Corke, T. C. (2004). Separation control on high angle of attack airfoil using plasma actuators. *AIAA journal*, 42(11), 2177-2184.
- Visbal, M., & Gaitonde, D. (2006, January). Control of vortical flows using simulated plasma actuators. In 44th AIAA aerospace sciences meeting and exhibit (p. 505).
- Greenblatt, D., Schneider, T., & Schüle, C. Y. (2012). Mechanism of flow separation control using plasma actuation. *Physics of Fluids*, 24(7), 077102.
- Suzen, Y., & Huang, G. (2006, January). Simulations of flow separation control using plasma actuators. In 44th AIAA Aerospace Sciences Meeting and Exhibit (p. 877).
- Peers, E., Huang, X., & Luo, X. (2009). A numerical model of plasma-actuator effects in flow-induced noise control. *IEEE Transactions on plasma science*, 37(11), 2250-2256.
- Roy, S., Zhao, P., DasGupta, A., & Soni, J. (2016). Dielectric barrier discharge actuator for vehicle drag reduction at highway speeds. *Aip Advances*, 6(2), 025322.
- Visbal, M., Gaitonde, D., & Roy, S. (2006, June). Control of transitional and turbulent flows using plasma-based actuators. In 36th AIAA Fluid Dynamics Conference and Exhibit (p. 3230).
- Boeuf, J. P., & Pitchford, L. C. (2005). Electrohydrodynamic force and aerodynamic flow acceleration in surface dielectric barrier discharge. *Journal of Applied Physics*, 97(10), 103307.
- Nishida, H., & Abe, T. (2011). Numerical analysis of plasma evolution on dielectric barrier discharge plasma actuator. *Journal of applied physics*, 110(1), 013302.
- Enloe, C. L., McLaughlin, T. E., Van Dyken, R. D., Kachner, K. D., Jumper, E. J., Corke, T. C., ... & Haddad, O. (2004). Mechanisms and responses of a dielectric barrier plasma actuator: Geometric effects. *AIAA journal*, 42(3), 595-604.
- Orlov, D. M. (2006). Modelling and simulation of single dielectric barrier discharge plasma actuators.
- Massines, F., Rabehi, A., Decomps, P., Gadri, R. B., Ségur, P., & Mayoux, C. (1998). Experimental and theoretical study of a glow discharge at atmospheric pressure controlled by dielectric barrier. *Journal of Applied Physics*, 83(6), 2950-2957.
- Roth, J. R., Sherman, D. M., & Wilkinson, S. P. (2000). Electrohydrodynamic flow control with a glow-discharge surface plasma. *AIAA journal*, 38(7), 1166-1172.
- Shyy, W., Jayaraman, B., & Andersson, A. (2002). Modeling of glow discharge-induced fluid dynamics. *Journal of applied physics*, 92(11), 6434-6443.
- Asada, K., & Fujii, K. (2010). Computational analysis of unsteady flow-field induced by plasma actuator in burst mode. In 5th Flow Control Conference (p. 5090).
- Asada, K., Nonomura, T., Aono, H., Sato, M., Okada, K., & Fujii, K. (2015). LES of transient flows controlled by DBD plasma actuator over a stalled airfoil. *International Journal of Computational Fluid Dynamics*, 29(3-5), 215-229.
- Corke, T. C., Enloe, C. L., & Wilkinson, S. P. (2010). Dielectric barrier discharge plasma actuators for flow control. *Annual review of fluid mechanics*, 42, 505-529.

18. Kotsonis, M., Ghaemi, S., Veldhuis, L., & Scarano, F. (2011). Measurement of the body force field of plasma actuators. *Journal of Physics D: Applied Physics*, 44(4), 045204.
19. Debien, A., Benard, N., David, L., & Moreau, E. (2012). Unsteady aspect of the electrohydrodynamic force produced by surface dielectric barrier discharge actuators. *Applied Physics Letters*, 100(1), 013901.
20. Aono, H., Sekimoto, S., Sato, M., Yakeno, A., Nonomura, T., & Fujii, K. (2015). Computational and experimental analysis of flow structures induced by a plasma actuator with burst modulations in quiescent air. *Mechanical Engineering Journal*, 15-00233.
21. Gibalov, V. I., & Pietsch, G. J. (2004). Dynamics of dielectric barrier discharges in coplanar arrangements. *Journal of Physics D: Applied Physics*, 37(15), 2082.
22. Boeuf, J. P., & Pitchford, L. C. (2005). Electrohydrodynamic force and aerodynamic flow acceleration in surface dielectric barrier discharge. *Journal of Applied Physics*, 97(10), 103307.
23. Likhanskii, A. V., Shneider, M. N., Macheret, S. O., & Miles, R. B. (2008). Modeling of dielectric barrier discharge plasma actuator in air. *Journal of Applied Physics*, 103(5), 053305.
24. Nishida, H., Nonomura, T., & Abe, T. (2014). Three-dimensional simulations of discharge plasma evolution on a dielectric barrier discharge plasma actuator. *Journal of Applied Physics*, 115(13), 133301.
25. Gaitonde, D. V., Visbal, M. R., & Rouy, S. (2008, September). Three-dimensional plasma-based stall control simulations with coupled first-principles approaches. In *ASME 2006 2nd Joint US-European Fluids Engineering Summer Meeting Collocated With the 14th International Conference on Nuclear Engineering* (pp. 1339-1356). American Society of Mechanical Engineers Digital Collection.
26. Orlov, D. M., Font, G. I., & Edelstein, D. (2008). Characterization of discharge modes of plasma actuators. *AIAA journal*, 46(12), 3142-3148.
27. Fujii, K. (2018). Three Flow Features behind the Flow Control Authority of DBD Plasma Actuator: Result of High-Fidelity Simulations and the Related Experiments. *Applied Sciences*, 8(4), 546.
28. See <http://www.siglo-kinema.com/bolsig.htm> for more information about the BOLSIG database.
29. Nishida, H., & Abe, T. (2011). Validation study of numerical simulation of discharge plasma on DBD plasma actuator. In *42nd AIAA Plasmadynamics and Lasers Conference in conjunction with the 18th International Conference on MHD Energy Conversion (ICMHD)* (p. 3913).
30. Fujii, K., Endo, H., & Yasuhara, M. (1992, January). Activities of computational fluid dynamics in Japan: compressible flow simulations. In *High performance computing* (pp. 139-161). John Wiley and Sons Ltd..
31. Fujii, K., & Obayashi, S. (1989). High-resolution upwind scheme for vortical-flow simulations. *Journal of Aircraft*, 26(12), 1123-1129.
32. Lele, S. K. (1992). Compact finite difference schemes with spectral-like resolution. *Journal of computational physics*, 103(1), 16-42.
33. Nishida, Hiroyuki, and Taku Nonomura. "Short Note: ADI-SGS scheme on ideal magnetohydrodynamics." *Journal of Computational Physics* 228.9 (2009): 3182-3188.
34. Kotsonis, M., & Ghaemi, S. (2012). Experimental and numerical characterization of a plasma actuator in continuous and pulsed actuation. *Sensors and Actuators A: Physical*, 187, 84-94.